Sensors and Materials, Vol. 38, No. 5 (2026) 2799–2812
MYU Tokyo

S & M 4470

Design of a Planar Metamaterial Absorber Capable of Optical Sensing from 500 to 3160 nm

Kao-Peng Min,[1] Yu-Ting Gao,[2] Cheng-Fu Yang,[3,4*]
Chi-Ting Ho,[5] Walter Water,[2] and Kao-Wei Min[6]

[1]College of Engineering, National Formosa University, Huwei, Yunlin 632, Taiwan
[2]Department of Electronic Engineering, National Formosa University, Yunlin 632, Taiwan
[3]Department of Chemical and Materials Engineering, National University of Kaohsiung, Kaohsiung 811, Taiwan
[4]Department of Aeronautical Engineering, Chaoyang University of Technology, Taichung 413, Taiwan
[5]Department of Mechanical Design Engineering, National Formosa University, Yunlin 632, Taiwan
[6]Department of Electrical Engineering, Cheng Shiu University, Kaohsiung 833, Taiwan

(Received November 18, 2025; accepted May 19, 2026)

Keywords: ultra-broadband absorber, optical absorber, numerical simulation, finite element method, COMSOL Multiphysics, multilayer thin-film scattering medium, electromagnetic field distribution

In this study, a planar multilayer metamaterial absorber capable of optical sensing across an ultra-broadband spectrum was designed and numerically analyzed using the finite element method implemented in the simulation software COMSOL Multiphysics (V6.0). The absorber consists of alternating metal–dielectric layers, with SiO_2 serving as the scattering medium to enhance electromagnetic coupling and impedance matching. A six-layer planar structure composed of V, Ge, Bi, and Co was first developed, achieving an average absorptivity of 94.56% within the 500–3160 nm wavelength range, though a slight absorption dip was observed between 400–500 nm. By introducing additional SiO_2 and Co layers to form an eight-layer configuration, the absorption bandwidth was broadened to 400–3700 nm with an average absorptivity of 93.69%. Furthermore, replacing Co with Ti extended the spectral response to 400–4000 nm, demonstrating enhanced optical adaptability. These findings indicate a design trade-off between absorption efficiency and bandwidth coverage, offering valuable insights for the development of high-performance optoelectronic and sensing devices based on planar metamaterial architectures.

1. Introduction

The interaction between light and matter has long been a fundamental and enduring research topic spanning physics, materials science, and optoelectronic engineering. With the rapid advancement of modern technology, the demand for optical components capable of achieving high efficiency across a broad spectral range has grown significantly. Among these components, ultra-broadband optical absorbers—devices capable of effectively absorbing electromagnetic waves over a wide range of frequencies—have attracted considerable research attention owing to

*Corresponding author: e-mail: cfyang@nuk.edu.tw
https://doi.org/10.18494/SAM6050

ISSN 0914-4935
https://myukk.org/

their potential applications in solar energy harvesting, thermal imaging, stealth technology, and optical sensing systems.[1,2] As performance requirements for advanced optical devices continue to rise across multiple disciplines, the role of broadband absorbers as critical elements in enhancing energy utilization has become increasingly important. In photovoltaic systems, such absorbers can improve solar cell efficiency by capturing energy from a broader portion of the solar spectrum.[3,4] In thermal and infrared sensing, they expand the detectable spectral range and improve sensitivity, enabling precise environmental and biomedical monitoring. Moreover, in military stealth technology, broadband absorbers help minimize radar and infrared signatures, enhancing concealment capabilities.

Despite their wide applicability, traditional optical absorption techniques still face challenges in achieving broadband performance. The inherent absorption bandwidth of a single material is typically narrow, and resonance-based absorbers often exhibit strong frequency selectivity, limiting their applicability across diverse wavelengths. Consequently, developing novel ultra-broadband optical absorbers has become a central research direction in photonic materials and sensing technologies. Conventional absorbers generally rely on the intrinsic optical properties of materials or resonance mechanisms, such as surface plasmon resonance (SPR), to achieve effective absorption at specific wavelength ranges. However, maintaining high absorption efficiency across a wide spectrum remains difficult owing to material and structural limitations. For instance, thin metallic film absorbers can perform well in the visible region but experience a sharp decline in absorptivity in the near- and mid-infrared regions.[5,6] To overcome these limitations, researchers have explored new material systems, innovative structural architectures, and advanced fabrication techniques to design absorbers capable of sustaining high efficiency from the visible-to-infrared spectral regions.

In recent years, multilayer metamaterial absorbers have emerged as a promising approach due to their design flexibility and potential for broadband absorption.[7] By precisely controlling the type, thickness, and stacking order of each film layer, it is possible to manipulate light propagation, interference, and absorption processes within the structure, enabling the efficient trapping of electromagnetic energy over wide spectral ranges. Metallic layers such as tungsten (W), nickel (Ni), cobalt (Co), and molybdenum (Mo) are often employed as high-loss absorbing layers or back reflectors because of their high free-electron density and dissipative characteristics, which facilitate localized surface plasmon resonance (LSPR) and impedance-matching absorption. Semiconductor or semimetal materials, including bismuth (Bi), germanium (Ge), and vanadium (V), can introduce multiple interference modes and improve spectral selectivity. On the other hand, low-loss dielectric materials such as silicon dioxide (SiO_2), titanium dioxide (TiO_2), and aluminum oxide (Al_2O_3) are effective for field confinement and dielectric resonance. When used as spacer or cavity layers, these materials enable multiple internal reflections, enhance optical path length, and increase overall absorption efficiency.

In practical configurations such as metal–dielectric–metal (MDM) or metal–semiconductor–metal (MSM) stacks, proper impedance matching at the interface can suppress reflection and achieve near-perfect absorption (absorption ≈ 1).[8] Such structures are particularly advantageous for infrared and solar spectrum coverage, where energy conversion and sensing performance are strongly dependent on broadband response. Moreover, the incorporation of dielectric scattering

media, especially SiO_2, has been shown to increase optical path length, enhance internal scattering, and strengthen the coupling between incident electromagnetic fields and localized modes, thus improving broadband absorption. In this study, we focus on the design and numerical simulation of a planar multilayer metamaterial absorber composed of alternating metallic and dielectric films for broadband optical sensing applications. Compared with many previously reported broadband absorbers that employ complex nanopatterned, graphene-assisted, or three-dimensional metamaterial architectures, the proposed absorber adopts a fully planar multilayer configuration, which is more compatible with conventional thin-film deposition processes and offers improved fabrication simplicity and scalability.[9-11]

In addition, the proposed structure only requires six functional layers to achieve a broadened operating range from 500 to 3160 nm while maintaining high average absorptivity. This demonstrates that efficient ultra-broadband absorption can be realized without relying on complex surface patterning or excessively multilayered designs, thereby providing an effective balance between structural simplicity, manufacturability, and broadband optical performance. Using COMSOL Multiphysics, a commercial finite element analysis platform, we constructed high-precision structural models and analyzed the optical absorption characteristics of two different multilayer configurations over a wide wavelength range. COMSOL's powerful simulation environment enables a detailed investigation of electromagnetic field distributions, plasmonic coupling effects, and impedance-matching behavior within the absorber structure. The initial design, composed of V, Ge, Bi, and Co, exhibited high average absorptivity in the 500–3000 nm range. To further extend the absorption bandwidth, additional dielectric and metallic layers were introduced, and titanium (Ti) was evaluated as a substitute material to optimize impedance matching and spectral response. Through structural parameter optimization, the absorber achieved a broadened operating range from 500 to 3160 nm, demonstrating a clear trade-off between average absorption efficiency and bandwidth extension. These findings highlight the feasibility of designing planar metamaterial absorbers that combine ultra-broadband absorption with sensing functionality, providing a theoretical and numerical foundation for next-generation optoelectronic and sensor-integrated materials.

2. Methodology

In this study, the simulation software COMSOL Multiphysics was employed to perform the numerical simulations and structural optimization of the proposed planar metamaterial optical absorber. The simulations were conducted using the finite element method, which enables the accurate modeling of electromagnetic field interactions within complex multilayer configurations. A systematic simulation procedure was followed to ensure both the computational accuracy and physical reliability of the obtained results. On the basis of the designed absorber configuration, a two-dimensional (2D) or three-dimensional (3D) geometric model was established within the COMSOL environment. The model precisely defined the geometry, layer thickness, and spatial dimensions of each component, with an air domain assigned at the top boundary to replicate real environmental conditions. Each structural layer—metallic, dielectric, or semiconductor—was then assigned optical constants, including refractive

index (n) and extinction coefficient (k), referring to the data obtained from published literature and verified experimental measurements.

To simulate electromagnetic wave propagation and absorption phenomena across the visible-to-infrared spectrum, input and output ports were defined. The original structure used in this study, illustrated in Fig. 1, comprises a six-layer planar configuration. From the bottom layer to the top, the materials and corresponding thicknesses are sequentially arranged as V (h1, 130 nm), Ge (h2, 45 nm), SiO_2 (h3, 130 nm), Bi (h4, 8 nm), SiO_2 (h5, 150 nm), and Co (h6, 1 nm). The input port served as the excitation interface for an incident plane wave covering the wavelength range of 500–3000 nm, while the output port was used to monitor transmitted waves and calculate the corresponding transmittance. The reflected power was derived simultaneously to determine the absorptivity spectrum via the relation

$$A(\lambda) = 1 - R(\lambda) - T(\lambda), \tag{1}$$

where A, R, and T denote absorption, reflection, and transmission, respectively. Since the proposed absorber structure exhibits periodic spatial arrangement, the Floquet periodic boundary condition was applied along the lateral sides of the unit cell to simulate an infinitely periodic array, as shown in Fig. 2(a). The Floquet wave vector (k-vector) was defined in the periodic port settings, which allowed the model to replicate the electromagnetic behavior of a large-scale periodic surface while substantially reducing computational costs. This approach ensures that the interaction between adjacent unit cells, crucial to optical sensing and field enhancement effects, is accurately captured without requiring excessive computational resources. Following the boundary and port configuration, meshing was performed to discretize the continuous geometry into finite elements, as depicted in Fig. 2(b). The mesh resolution plays a critical role in balancing accuracy and efficiency: finer mesh elements were applied to metal–dielectric interfaces where electromagnetic field gradients are strongest, ensuring the precise resolution of LSPR effects and near-field energy confinement. The mesh convergence was verified by monitoring the absorption spectral variation under successive mesh refinements until numerical stability was achieved.

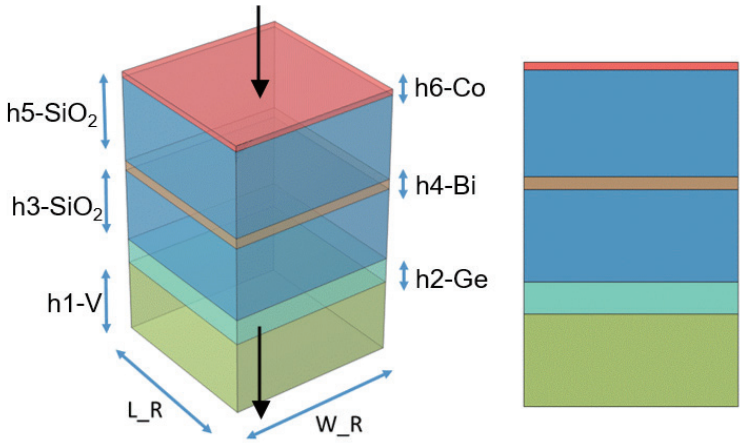

Fig. 1. (Color online) Optical input port and optical output port settings.

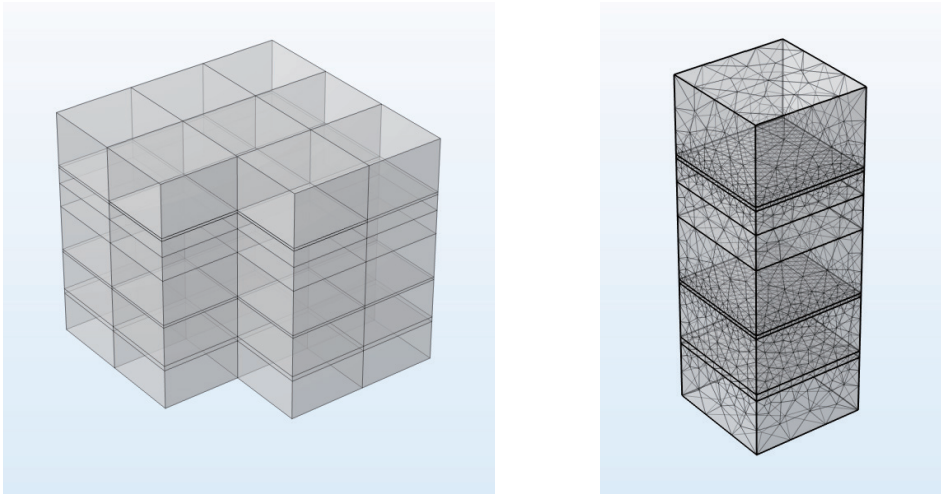

(a) (b)

Fig. 2. (Color online) (a) Periodic array extension model and (b) model meshing.

After the structural model was established, meshing was performed to discretize the geometry into finite elements, as shown in Fig. 2(b). A total of 2757 elements were generated, including 1425 mesh nodes, 2757 triangular elements, 347 edge elements, and 16 boundary loops. The mesh quality was evaluated using the skewness metric, yielding a minimum quality of 0.5553 and an average quality of 0.8168, indicating good mesh uniformity and geometric consistency. The minimum element area was 0.001622 nm^2 and the total meshed surface area reached 188700 nm^2, confirming that the mesh resolution was sufficiently fine to capture localized electromagnetic field variations while maintaining numerical stability. This meshing accuracy provides a reliable basis for calculating the reflectance, transmittance, and absorptivity spectra. Although this study is mainly focused on numerical simulation and structural optimization, the proposed multilayer absorber can be practically fabricated using existing thin-film deposition technologies such as electron-beam evaporation and thermal evaporation.

The planar multilayer configuration simplifies the fabrication process compared with complex nanopatterned metamaterials and improves scalability and reproducibility. In future work, experimental validation can be performed by fabricating V/Ge/SiO_2/Bi/Co multilayer films on suitable substrates and measuring the corresponding absorption spectra. Several practical fabrication factors should also be considered. Fabrication tolerances may slightly affect layer thicknesses and cause minor shifts in resonance wavelength and absorption bandwidth. However, because the proposed absorber relies on coupled impedance matching and multilayer resonance effects over a broad spectral range, moderate dimensional variations are not expected to significantly degrade performance. Surface roughness at metal–dielectric interfaces may affect plasmonic coupling and optical scattering, but optimized deposition conditions can improve film uniformity. In addition, oxidation effects in ultrathin metallic layers may alter the optical properties during long-term operation. This problem can be reduced by using protective dielectric capping layers or controlled vacuum fabrication processes. Therefore, the proposed

structure demonstrates good potential for future experimental realization and practical optical sensing applications.

3. Simulation Results and Discussion

This multilayer design integrates both metallic and dielectric components to achieve broadband optical absorption and enhanced electromagnetic field confinement across the visible-to-infrared spectrum. The bottom layer of V, with a thickness of 130 nm, functions as the optical reflective layer because of its high reflectivity and excellent electrical conductivity. This layer effectively prevents light transmission and creates a back-reflection interface, thereby enhancing the overall light absorption efficiency of the upper layers.[12] Our simulation results (not shown here) indicate that a V layer thicker than 100 nm is required to achieve near-total reflection; therefore, 130 nm was selected as the optimal thickness to ensure complete reflectivity and stable optical confinement. The 45-nm-thick Ge layer serves as the primary absorbing layer. As a direct bandgap semiconductor, Ge exhibits strong light absorption capability through interband transitions, enabling efficient photon-to-energy conversion within specific wavelength ranges.[13]

The two SiO_2 dielectric layers, with thicknesses of 130 nm (upper) and 150 nm (lower), together form an optical cavity. By tuning their refractive indices and thicknesses, the resonant wavelength and mode distribution can be precisely controlled, thereby enhancing interference strength and absorption efficiency.[14] The 8 nm Bi layer, a semimetal, is incorporated to improve impedance matching and electromagnetic coupling efficiency owing to its tunable dielectric properties and distinctive plasmonic behavior. Finally, the 1 nm Co top layer serves to induce surface plasmon resonance (SPR). This ultrathin metallic film significantly enhances the localized electromagnetic field intensity at the interface, promoting near-field absorption and nonradiative energy dissipation. Overall, the proposed multilayer structure synergistically integrates metal–dielectric–semiconductor–semimetal components, combining SPR and Fabry–Pérot interference mechanisms to achieve efficient light trapping and energy conversion across a broad spectral range.

The analysis is first focused on the Ge (h2) layer, as illustrated in Fig. 3(a). A parametric sweep was conducted for Ge layer thicknesses ranging from 35 to 55 nm in 5 nm increments, across a wavelength range of 400–3500 nm. The results clearly show that as the Ge layer thickness increases from 35 to 55 nm, the short-wavelength absorption edge initially blue-shifts from 580 nm (at 35 nm thickness) to 500 nm (at 45 nm thickness), after which it remains almost unchanged. Moreover, the long-wavelength absorption edge exhibits a redshift from 3020 to 3180 nm. This behavior indicates that increasing the Ge layer thickness broadens the high-absorptivity bandwidth (defined as the wavelength range where absorptivity > 0.9). However, a notable drop in absorptivity is observed within the 900–1700 nm range as the thickness increases. This reduction is attributed to optical interference effects and phase mismatches within the multilayer cavity, which weaken the field confinement at these mid-infrared wavelengths. Therefore, a Ge layer thickness of 45 nm is determined to be optimal, as it provides the widest effective absorption bandwidth and maintains strong, uniform absorptivity across the visible-to-infrared spectrum.

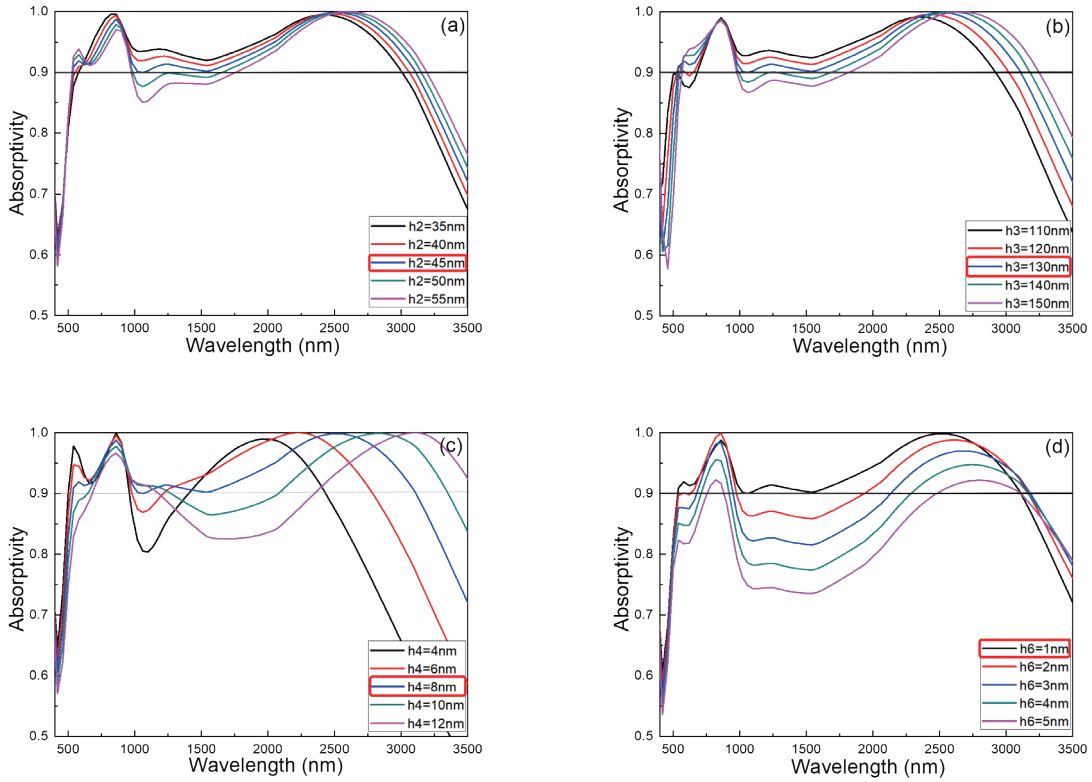

Fig. 3. (Color online) Effects of the thicknesses of (a) h2, (b) h3, (c) h4, and (d) h6 layers on absorption spectra of the investigated absorbers.

In this study, the determination of the optimal layer thicknesses was based primarily on two evaluation criteria: the effective absorption bandwidth and the average absorptivity. The effective absorption bandwidth was defined as the wavelength range where the absorptivity exceeds 0.9, since this condition represents efficient broadband optical absorption suitable for sensing and photothermal applications. Therefore, a wider wavelength range with absorptivity above 0.9 indicates superior broadband performance. At the same time, the average absorptivity across the operating spectral range was also considered to ensure stable and efficient light absorption over the entire visible-to-infrared spectral region. Consequently, the optimal thickness for each layer was selected by balancing both the broadband absorption range and the overall absorption efficiency rather than relying solely on peak absorptivity at a single wavelength. The next optimization is that of the SiO_2 (h3) layer, as presented in Fig. 3(b). A similar sweep was carried out for SiO_2 layer thicknesses between 110 and 150 nm in 10 nm increments, over the same 400–3500 nm wavelength range. As the SiO_2 layer thickens from 110 to 130 nm, the short-wavelength absorption edge initially blue-shifts from 700 to 500 nm, reflecting stronger cavity confinement and enhanced constructive interference between the dielectric and metal layers. When the thickness increases beyond 130 nm, however, the spectrum redshifts to approximately 580 nm, indicating destructive interference and phase retardation effects that degrade overall absorption. Simultaneously, the long-wavelength edge shifts from

2980 to 3260 nm, a result of the increased optical path length within the thicker dielectric layer. The results in Fig. 3(b) clearly show that increasing the SiO_2 layer thickness up to 130 nm significantly enhances the broadband absorption region. Beyond this value, at 140 and 150 nm, absorptivity within 1000–1700 nm drops to below 0.9, suggesting suboptimal impedance matching and reduced energy confinement. Consequently, a 130 nm SiO_2 layer is selected as the optimal configuration, ensuring a balance between resonance control, interference enhancement, and absorption stability.

The coupled optimization of the Ge absorbing layer (h2) and the SiO_2 cavity layer (h3) demonstrates how fine-tuning layer thicknesses can precisely regulate optical interference, plasmonic coupling, and impedance matching within the absorber. This optimized configuration enables maximum broadband absorption performance, making it highly suitable for optical sensing, infrared detection, and energy-harvesting applications where sensitivity and spectral coverage are critical. The next parameter analyzed is the thickness of the h4 Bi layer, as shown in Fig. 3(c). A thickness sweep ranging from 4 to 12 nm was performed with a step size of 2 nm. As the thickness of the Bi layer increased from 4 to 12 nm, the absorption spectrum at the short-wavelength region exhibited a redshift from 420 to 880 nm, while the long-wavelength edge shifted rapidly from 2520 nm to beyond the analytical range (3500 nm). Interestingly, as the Bi layer thickness increased from 4 to 12 nm, a distinct absorption dip (absorptivity < 0.900) emerged near 1100 nm, and the magnitude of this dip became more pronounced with increasing Bi layer thickness. Furthermore, when the Bi layer thickness exceeded 8 nm, an additional low-absorptivity region appeared between 1200 and 2400 nm. These results indicate that the absorber will achieve its optimal broadband performance when the Bi layer thickness is 4 nm, as thicker Bi layers introduce interference effects that disrupt the high-absorptivity bandwidth.

For the h5 SiO_2 layer thickness analysis (not shown here), a similar parametric sweep was performed over a range of 130–170 nm with a 10 nm step size. As the SiO_2 layer thickness increased from 130 to 170 nm, the short-wavelength absorption edge redshifted from 460 to 800 nm, indicating a stronger cavity resonance effect. However, a notable absorption dip near 1100 nm became more pronounced as the thickness increased, and when the SiO_2 layer thickness reached or exceeded 150 nm, this dip caused the absorptivity to fall below the desired 0.900 threshold. Moreover, the long-wavelength edge exhibited only a slight redshift from 3020 to 3160 nm. On the basis of these observations, the optimal SiO_2 layer thickness was determined to be 150 nm, at which a balanced trade-off between broadband absorption and spectral uniformity can be achieved. The combined analysis of the h4 and h5 layers demonstrates the critical effects of both metallic and dielectric thicknesses on plasmonic coupling and interference resonance within the absorber structure. The proper tuning of these layers ensures enhanced optical confinement, minimized reflection losses, and wider absorption bandwidth across the visible-to-infrared spectrum.

Finally, the effect of the h6 Co layer thickness on the absorption spectrum was analyzed, as illustrated in Fig. 3(d). The Co layer thickness was varied from 1 to 5 nm with a 1 nm step size. When the h6 layer thickness was 1 nm, the absorber exhibited consistently high absorptivity (>0.900) across a broad spectral range from 500 to 3160 nm, indicating efficient light trapping and minimal reflection losses. However, as the thickness increased to 2 nm or greater, distinct

low-absorptivity dips appeared in the 1100–2000 nm region, with the overall absorptivity progressively decreasing as the Co layer became thicker. This behavior can be attributed to the increased optical loss and altered impedance matching caused by the excessive thickness of the metallic Co layer. A thicker metal layer enhances reflection at the interface and weakens the LSPR coupling with the adjacent dielectric layers, thereby reducing the overall absorption efficiency in the near-infrared region. Consequently, the optimal thickness for the h6 Co layer was determined to be 1 nm, as it ensures a balanced plasmonic resonance and superior broadband absorption performance across the visible-to-infrared spectrum. The h6 Co layer plays a critical role in fine-tuning the impedance matching and resonance balance within the absorber stack. Maintaining a minimal Co layer thickness not only preserves high absorptivity over a wide wavelength range but also stabilizes the optical response, making it ideal for broadband photonic and energy-harvesting applications.

Figure 4 presents the optical impedance matching characteristics of the designed absorber under the optimized structural parameters, within the 500–3800 nm wavelength range, where the black curve represents the real part of the impedance and the red curve represents the imaginary part. When the real part approaches 1 and the imaginary part approaches 0, the structure achieves near-perfect impedance matching with free space. This condition effectively minimizes reflection losses and facilitates the efficient coupling of the incident optical energy into the absorber layer, thereby enabling high absorption performance across a broad spectral range. The results clearly indicate that, throughout most of the wavelength range, the real part of the impedance remains close to 1, while the imaginary part remains near 0, signifying excellent impedance matching. Notably, at the wavelengths corresponding to the main absorption peaks, the impedance matching is particularly strong, confirming that the designed multilayer structure provides superior broadband impedance compatibility.

As shown in Fig. 4, within the range of 500–3160 nm, the real part of impedance consistently remains near 1 and the imaginary part remains close to 0, corresponding well with the spectral

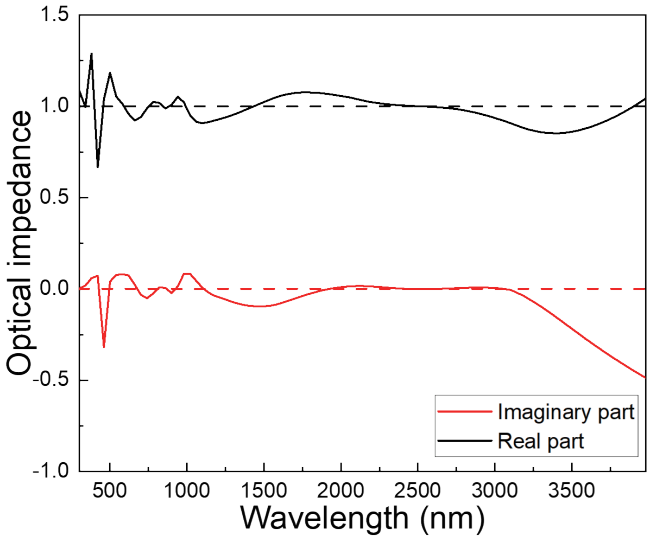

Fig. 4. (Color online) Optical impedance of the investigated absorber.

regions of high absorptivity (>0.900). This correlation verifies that the absorber's outstanding performance stems from the synergistic impedance matching among its metallic, dielectric, and semiconductor layers, which effectively suppresses reflection and maximizes light confinement. Such impedance-matched design principles are crucial for realizing ultra-broadband optical absorbers, as they ensure that incoming electromagnetic waves are seamlessly transmitted into the multilayer stack, converted into localized plasmonic and resonant energy modes, and efficiently dissipated through absorption rather than reflection.

To verify that the absorber designed in this study exhibits high absorption efficiency, we analyzed its optical absorption, reflection, and transmission characteristics across the 400–3600 nm wavelength range. As shown in Fig. 5, the transmissivity remains nearly zero throughout the entire spectral range, indicating that the bottom V metallic layer effectively blocks incident light from penetrating through the structure. This confirms that the vanadium layer functions as an optical reflector, redirecting unabsorbed light back into the upper layers, thereby reinforcing internal interference and absorption. Furthermore, the results in Fig. 5 demonstrate that within the same wavelength range, the sum of absorptivity and reflectivity is consistently close to unity (1), verifying the energy conservation and numerical accuracy of the simulation. This relationship also highlights that nearly all incident optical energy is either reflected or absorbed with negligible transmission loss. The near-zero transmission and complementary absorptivity–reflectivity behavior collectively confirm that the proposed multilayer structure achieves excellent light-trapping capability and broadband optical absorption. This performance arises from the synergistic interaction between the reflective metallic base and the resonant upper layers, which together enhance the optical path length, field confinement, and impedance matching across the visible-to-infrared spectrum. As a result, the designed absorber demonstrates strong potential for photothermal conversion, infrared detection, and solar energy harvesting applications where broadband, high-efficiency absorption is crucial.

To further investigate the underlying mechanisms responsible for the high absorption observed in the 500–3160 nm range, we conducted transverse electric (TE) and field transverse

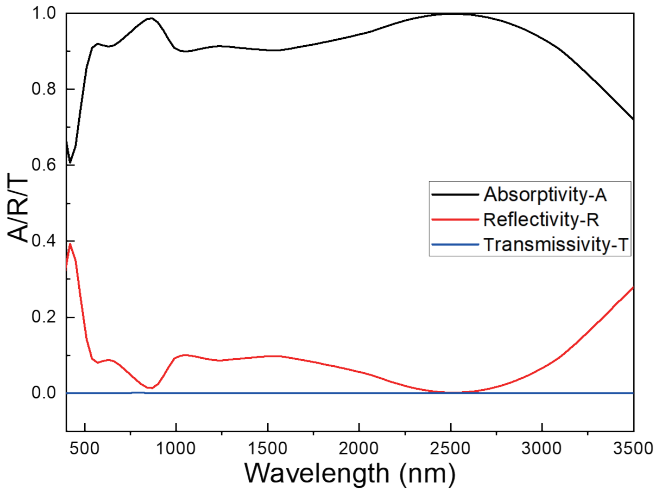

Fig. 5. (Color online) Optical absorption, reflection, and transmission characteristics of the investigated absorber.

magnetic (TM) analyses at specific wavelengths corresponding to the main absorption peaks identified in Fig. 5, namely, 580, 860, 1220, and 2500 nm. These selected wavelengths represent characteristic resonant points where the structure exhibits distinct absorption enhancement behaviors. As shown in Fig. 6, at 580 nm, the electric field intensity is strongly concentrated at the metal–dielectric interfaces and confined primarily within the h3 SiO_2 dielectric layer, clearly demonstrating the coupled effects of LSPR and Fabry–Pérot (FP) cavity resonance. This coupling enhances light–matter interaction and promotes efficient energy trapping near the interface. At longer wavelengths (860, 1220, and 2500 nm), pronounced localized electromagnetic fields appear near the upper metallic layers and gradually penetrate into the intermediate dielectric region. The LSPR-induced resonances at the metal–semiconductor and metal–dielectric boundaries result in strong local field enhancement, while the distribution of the electric field becomes more uniform and extends deeper toward the lower layers.

The field distribution results further clarify the coupling mechanisms responsible for the ultra-broadband absorption behavior. At shorter wavelengths, the electric fields are mainly concentrated near the metal–dielectric interfaces, indicating that LSPR-induced near-field confinement dominates the absorption process. As the wavelength increases, the electromagnetic fields gradually penetrate deeper into the multilayer cavity, demonstrating stronger FP resonance and phase retardation effects within the dielectric layers. The increased optical path length resulting from multiple reflections and phase accumulation enhances the interaction between incident light and the multilayer structure, thereby improving energy confinement and absorption efficiency. Moreover, the coexistence of localized plasmonic resonance and cavity interference enables efficient mode coupling between adjacent layers, allowing electromagnetic energy to be continuously transferred and dissipated within the metallic absorbing regions. The energy dissipation pathways are therefore associated with both plasmonic loss at the metal interfaces and resonance-enhanced optical confinement inside the dielectric cavity layers, which collectively contribute to the observed broadband high-absorptivity characteristics.

This behavior indicates efficient multilayer optical coupling, where plasmonic and interference modes jointly enhance broadband absorption. The magnetic field distributions are mainly concentrated within the h2 (Ge) and h3 (SiO_2) layers, further confirming the resonant coupling between LSPR excitation and cavity interference modes. This coupling leads to strong electromagnetic energy confinement and suppressed reflection, which are key contributors to

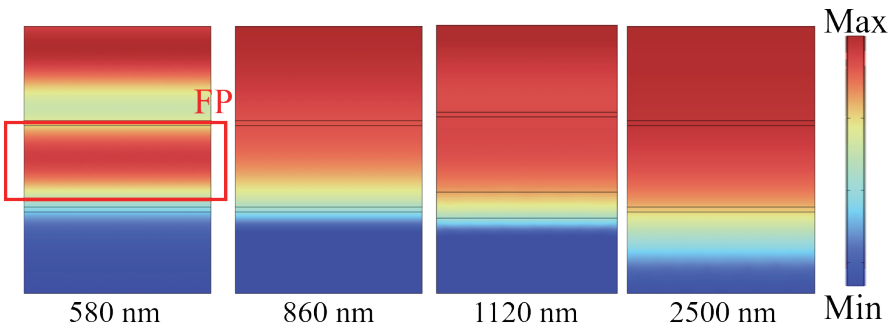

Fig. 6. (Color online) Distributions of electric field intensities and absorption at different wavelengths.

the observed ultra-broadband and high-absorptivity characteristics of the designed structure. Overall, these results verify that the superior absorption performance arises from the synergistic interaction of LSPR and FP resonance mechanisms, where surface plasmon excitation enhances near-field confinement, and the optical cavity effect sustains prolonged light–matter interaction across the multilayer architecture. Such dual-resonance coupling mechanisms make the proposed absorber highly effective for applications requiring broadband photothermal conversion, infrared sensing, and energy-harvesting systems.

Figure 7(a) illustrates the absorption spectra of the proposed optical absorber under different incident angles (θ) for TE polarization conditions. In TE polarization, the electric field is perpendicular to the plane of incidence. The angle- and polarization-dependent responses were analyzed to evaluate the broadband optical stability of the absorber under oblique incidence. As shown in Fig. 7(a), when the incident angle increases from normal incidence to approximately 40°, the absorption spectra exhibit only slight variations in spectral shape and absorptivity. The absorber still maintains high absorption efficiency within the broadband wavelength range from approximately 500 to 3500 nm, demonstrating excellent angular insensitivity within this range. However, when the incident angle further increases from 50 to 80°, a notable reduction in absorptivity occurs, particularly within the shorter wavelength region from 500 to 2000 nm. Although the absorption performance decreases at incident angles between 50 and 60°, relatively high absorptivity can still be maintained in certain wavelength regions. For example, at 60° incidence, an absorption peak close to 0.9 is still observed near 3000 nm.

When the incident angle reaches 70 and 80°, the absorption degradation becomes more significant and is accompanied by spectral distortion. Under large-angle incidence, the optical interaction path and effective optical thickness within the multilayer structure are altered, causing the matching conditions for SPR and FP cavity resonance to deviate from their optimal states. In particular, large incident angles reduce the effective electric field component parallel to the metallic interfaces, thereby reducing SPR excitation efficiency. In addition, variations in effective dielectric constant and impedance-matching conditions increase reflection losses instead of electromagnetic absorption. These results indicate that the proposed absorber exhibits

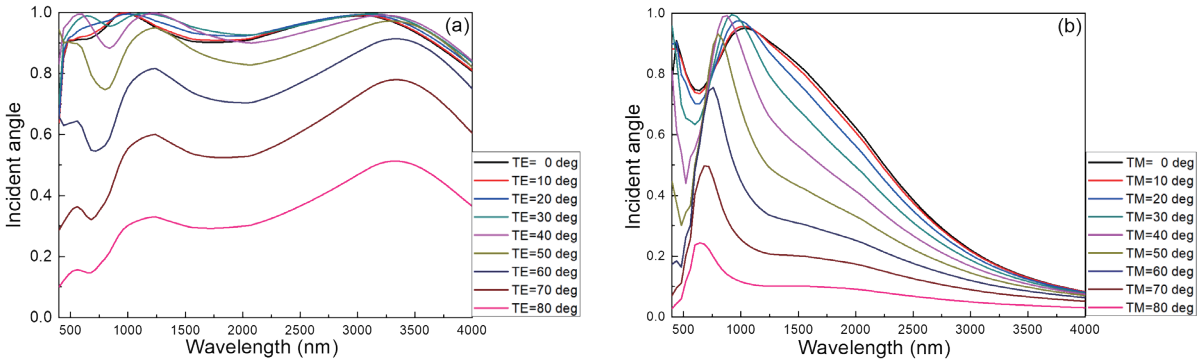

Fig. 7. (Color online) Absorption spectra of the proposed optical absorber under different incident angles (θ) for (a) TE and (b) polarization conditions.

excellent broadband absorption performance within the TE-polarized incident angle range from 0 to 40°. Although the absorption efficiency decreases at larger incident angles, the structure still maintains moderate absorption capability within certain long-wavelength regions.

Figure 7(b) presents the absorption spectra of the proposed absorber under TM polarization at different incident angles. The absorber exhibits near-perfect absorption in the visible and partial near-infrared regions, especially below approximately 1000 nm, where the absorptivity approaches 100%. Under normal incidence (0°), the TM-polarized absorption spectrum shows broadband absorption with absorptivity close to 1.0, consistent with the TE-polarized response and the polarization-insensitive behavior expected for isotropic planar structures. As the incident angle increases, the TM-polarized absorption spectra gradually change. Below 30°, the short-wavelength region (500–1000 nm) still maintains relatively high absorptivity, although the absorption peaks slightly shift toward shorter wavelengths and the absorptivity above 1500 nm decreases. This indicates that the structure can still effectively absorb short-wavelength photons under small oblique incidence, while long-wavelength absorption becomes more incident-angle-sensitive.

When the incident angle exceeds 40°, the TM-polarized spectra show significant distortion. The absorption peaks exhibit obvious blue shifts, accompanied by a rapid reduction in overall absorptivity. At 80° incidence, only a weak absorption peak with absorptivity around 0.2 remains within the 500–800 nm range, while absorption above 1000 nm is nearly suppressed. The interaction between TM-polarized light and the multilayer metal–dielectric structure involves several coupled mechanisms. TM-polarized waves possess an electric field component normal to the metal–dielectric interface, enabling the efficient excitation of surface plasmon polaritons (SPPs). However, the excitation efficiency strongly depends on the incident angle. At large incident angles, the optical path length, effective dielectric constant, and impedance-matching conditions deviate from their optimal states, increasing reflection losses. In addition, the FP resonance condition is highly incident-angle-dependent, and large incident angles can weaken or shift the resonance modes, thereby reducing absorption efficiency. These combined effects result in the significant degradation of absorption performance under large-angle TM-polarized incidence.

4. Conclusions

The planar metamaterial absorber proposed in this study exhibits outstanding ultra-broadband absorption performance across the 500–3160 nm range, as confirmed by finite element simulations using COMSOL Multiphysics. The optimized multilayer configuration composed of V, Ge, SiO_2, Bi, and Co achieves an average absorptivity exceeding 0.93 throughout the target spectrum. The bottom V layer ensures strong reflection and electromagnetic confinement, while the intermediate Ge and Bi layers enhance light absorption and impedance matching. The SiO_2 dielectric layers further regulate the optical cavity effect, amplifying FP resonance and constructive interference. The TE-mode electric field analysis reveals that the broadband absorption originates from the synergistic coupling between LSPR and FP resonances. At shorter wavelengths (around 580 nm), strong electric field confinement is

observed at the metal–dielectric interface and within the h_3 dielectric layer, confirming the coexistence of LSPR and FP resonance effects. As the wavelength increases to 860, 1220, and 2500 nm, the localized electromagnetic fields gradually penetrate into deeper layers, forming a more uniform and intensified field distribution. Moreover, impedance analysis indicates near-perfect matching with free space, minimizing reflection and maximizing energy coupling into the absorber. These combined effects result in efficient light trapping and enhanced electromagnetic energy confinement, establishing the designed absorber as a promising candidate for advanced applications in optical sensing, photothermal conversion, and infrared detection technologies.

Acknowledgments

This work is supported by Summit-Tech Resource Corp. and by projects under NSTC 113-2221-E-390-011 and NSTC 114-2622-E-390-001. We would be like to thank Pitotech Co., Ltd., for their help in instruction on the use of COMSOL Multiphysics® software.

References

1 S. Shamim, A. S. M. Mohsin, M. M. Rahman, and M. B. H. Bhuian: Heliyon **10** (2024) e33272.
2 M. A. Islam, M. Hasan, and R. Ahmed: Opt. Continuum **4** (2025) 756.
3 G. Peng, W. Z. Li, L. C. Tseng, and C. F. Yang: Nanomaterials **13** (2023) 766.
4 C. F. Yang, C. H. Wang, P. X. Ke, T. H. Meen, and K. K. Lai: Nanomaterials **14** (2024) 930.
5 N. Mishra, A. Chandra, R. Kumar, M. Karthikeyan, P. Pareek, and L. Singh: Mater. Sci. Eng. B **313** (2025) 117917.
6 M. R. Rakhshani, H. Karimi, and A. Ghaffari: Sci. Rep. **15** (2025) 23594.
7 Y. H. Nam, H. D. Um, K. T. Park, S. M. Shin, J. W. Baek, M. J. Park, J. Y. Jung, K. Zhou, S. W. Jee, Z. Guo, and J. H. Lee: J. Korean Phys. Soc. **60** (2012) 1944.
8 S. Tian, J. Wang, S. Sun, M. He, Y. Mao, Y. Gao, and P. Ding: Results Phys. **49** (2023) 106485.
9 C. T. Liao, K. P. Min, Y. J. Li, L. C. Tseng, C. T. Ho, and C. F. Yang: Sens. Mater. **35** (2025) 4285.
10 C. T. Liao, K. P. Min, Y. C. Tsai, L. C. Tseng, C. T. Ho, and C. F. Yang: Sens. Mater. **35** (2025) 4297.
11 K. P. Min, Y. T. Gao, C. F. Yang, W. Water, and C. T. Ho: Photonics **13** (2026) 86.
12 N. I. Landy, S. Sajuyigbe, J. J. Mock, D. R. Smith, and W. J. Padilla: Phys. Rev. Lett. **100** (2008) 207402.
13 S. M. Sze, Y. Li, and K. K. Ng: Physics of Semiconductor Devices (Wiley, Hoboken, NJ, USA, 2021) 4th ed.
14 P. Yeh: Optical Waves in Layered Media, Hoboken, (Wiley, NJ, USA, 2005) 2nd ed.